ARTICLE   OPEN

Check for updates

Coexistence of nontrivial topological properties and strong ferromagnetic fluctuations in quasi-one-dimensional $A_2Cr_3As_3$

Chenchao Xu[1], Ninghua Wu[1], Guo-Xiang Zhi[1], Bing-Hua Lei[2], Xu Duan[3,4,5], Fanlong Ning[1,6], Chao Cao [3✉] and Qijin Chen[1,7✉]

Superconductivity in crystals without inversion symmetry has received extensive attention due to its unconventional pairing and possible nontrivial topological properties. Using first-principles calculations, we systemically study the electronic structure of noncentrosymmetric superconductors $A_2Cr_3As_3$ (A = Na, K, Rb, and Cs). Topologically protected triply degenerate points connected by one-dimensional arcs appear along the C_3 axis, coexisting with strong ferromagnetic (FM) fluctuations in the non-superconducting state. Within random phase approximation, our calculations show that strong enhancements of spin fluctuations are present in $K_2Cr_3As_3$ and $Rb_2Cr_3As_3$ and are substantially reduced in $Na_2Cr_3As_3$ and $Cs_2Cr_3As_3$. Symmetry analysis of pairing gap $\Delta(\mathbf{k})$ and spin–orbit coupling $\mathbf{g_k}$ suggest that the arc surface states may also exist in the superconducting state, giving rise to possible nontrivial topological properties.

INTRODUCTION

Materials with nontrivial topological properties have been extensively studied over the past two decades. Initially, comprehensive attentions were paid to topological insulators (TIs)[1–3], which have an insulating gap in the bulk and metallic surface states at the boundary. Fully gapped superconductors with the topological protected gapless surface mode, a close analogy with TI, are regarded as promising candidates for hosting Majorana fermions. Since the discovery of Weyl, Dirac, nodal line semimetals, and triply degenerate point (TP) topological metals[4–15], it was shown that gapless systems can possess novel topology as well. Simultaneously, it is also possible for superconductors with nodes (e.g., $CePt_3Si$, UPt_3) to have topologically protected edge states, which are guaranteed by momentum-dependent topological numbers[16–18]. Among these exotic superconductors, nodal noncentrosymmetric superconductors (NCSs) with topological stable nodes have fascinating properties, i.e., the zero-energy boundary modes[19,20]. These zero-energy boundary modes are believed to be closely associated with the nodal gap structure via the so-called bulk–boundary correspondence[21].

The Cr-based arsenides $A_2Cr_3As_3$ (A = Na, K, Rb, and Cs) are of great interest in terms of low dimensionality, strong ferromagnetic (FM) fluctuations, and noncentrosymmetric superconductivity. Their nodal, unconventional superconductivity was suggested by London penetration depth, nuclear magnetic resonance (NMR), muon spin spectroscopy, and specific-heat measurements[22–29]. Besides, spin–orbit coupling (SOC) has a remarkable effect on β and γ bands in $K_2Cr_3As_3$ with a band spin-splitting much larger than the superconducting gap[30]. The coalescence of considerable SOC effect and strong FM fluctuations in $A_2Cr_3As_3$ NCSs is crucial to the superconducting pairing symmetry, leading to a predominant spin–triplet component, which is distinguished from the pairing in the isotropic channel of an usual s-wave superconductor. More recently, NMR experiments on $A_2Cr_3As_3$ suggest that the compounds in this family are possibly a solid-state analog of superfluid ^3He, implying that the unconventional superconductor $A_2Cr_3As_3$ may host nontrivial topological properties[31]. In addition, the NMR measurements of $Cs_2Cr_3As_3$ were distinct from that of $K_2Cr_3As_3$ ($Rb_2Cr_3As_3$), which displayed suppression of FM fluctuations in the former[32]. Therefore, a systematic study of the SOC effect, the topological properties as well as the FM fluctuations, and a thorough comparison among the family is in need.

In this article, we report our latest first-principles results on the $A_2Cr_3As_3$ family. Our results show: (1) The variations in band structures and Fermi surfaces (FSs) due to alkaline element substitution do not show apparent systematic behavior; (2) The anti-symmetric spin–orbit coupling (ASOC) splitting is the largest in $K_2Cr_3As_3$, but its effect is most significant in $Cs_2Cr_3As_3$ and enhances its one dimensionality; (3) All compounds of this family host TPs along Γ–A and the surface states emerging from the TPs form one-dimensional (1D) Fermi arcs; (4) The magnetic susceptibility spectrum exhibits a strong peak of the spin susceptibilities at the Γ point in $K_2Cr_3As_3$, followed by $Rb_2Cr_3As_3$, while in $Na_2Cr_3As_3$ and $Cs_2Cr_3As_3$ the enhancement of spin susceptibilities at the Γ point is not obvious. Inclusion of dynamic self-energy due to spin fluctuation does not alter the topology of electronic spectrum, and thus the existence of TPs is robust against the dynamic spin fluctuation at random phase approximation (RPA) level. Finally, we discuss the possibility of the existence of topologically stable arc states in the superconducting phase.

RESULTS

Electronic structure and topological properties

The crystal structure and Brillouin zone of $K_2Cr_3As_3$ are illustrated in Fig. 1a, b. For the compounds of this family, each primitive unit cell consists of $[(Cr_6As_6)]_\infty$ sub-nanotube along the c axis forming a

[1]Department of Physics, Zhejiang University, 310027 Hangzhou, China. [2]CAS Key Laboratory of Functional Materials and Devices for Special Environments, Xinjiang Technical Institute of Physics and Chemistry, CAS, Xinjiang Key Laboratory of Electronic Information Materials and Devices, 40-1 South Beijing Road, 830011 Urumqi, China. [3]Condensed Matter Group, Department of Physics, Hangzhou Normal University, 311121 Hangzhou, China. [4]Westlake University, Hangzhou, Zhejiang, China. [5]Department of Physics, Fudan University, Shanghai, China. [6]Collaborative Innovation Center of Advanced Microstructures, Nanjing University, 210093 Nanjing, China. [7]Shanghai Branch, National Laboratory for Physical Sciences at Microscale and Department of Modern Physics, University of Science and Technology of China, 201315 Shanghai, China. ✉email: ccao@hznu.edu.cn ; qchen@zju.edu.cn
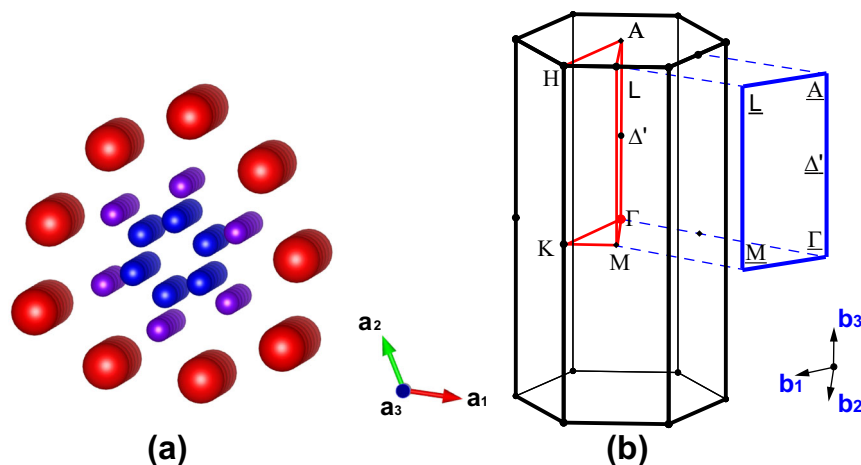
npj nature partner journals

Fig. 1 Geometry and Brillouin zone. a Crystal structure of $A_2Cr_3As_3$. The red, blue, and purple are alkali, chromium, and arsenic atoms, respectively. **b** Brillouin zone (BZ) and high symmetry points. The blue lines represent the [010] surface BZ.

quasi-one-dimensional (Q1D) structure[29,33–36]. In contrast to ACr_3As_3 ($A = K$, Rb)[37–40], the A^+ ions around the $[(Cr_6As_6)]_\infty$ sub-nanotube break the inversion symmetry, rendering $A_2Cr_3As_3$ noncentrosymmetric (with symmetry D_{3h}, space group 187). From $Na_2Cr_3As_3$, $K_2Cr_3As_3$, $Rb_2Cr_3As_3$ to $Cs_2Cr_3As_3$, the lattice expands in-plane while the average Cr-Cr bond length barely changes, implying increased distances between the $[(Cr_6As_6)]_\infty$ tubes.

Despite this systematic structural variation, the band structures (Fig. 2a–d) of $A_2Cr_3As_3$ around the Fermi level resemble each other and do not exhibit apparent change except for $Cs_2Cr_3As_3$. In the absence of SOC, the α and β bands cross the Fermi level along Γ–A, forming two Q1D FSs (see Supplementary Fig. 1 for details). In contrast, the γ band forms one three-dimensional (3D) FS around the Γ point (Fig. 3a–c) for $Na_2Cr_3As_3$ and $Rb_2Cr_3As_3$, similar to $K_2Cr_3As_3$[30,41]. For $Cs_2Cr_3As_3$, it is worth noting that the γ band do not cross the Fermi level in the $k_z = 0$ plane. As a result, this band forms one deformed Q1D FS. In addition, a fourth band (γ') around the Γ point emerges, creating a new 3D FS (Fig. 3d). Once the SOC effect is included, for all members in this family, the β and γ bands further split due to the ASOC effect.

Remarkably, the compounds of $A_2Cr_3As_3$ host TPs along Γ–A. In particular, the TPs in $Na_2Cr_3As_3$ (8 meV above the Fermi level ϵ_F) and $K_2Cr_3As_3$ (0.6 meV below ϵ_F) around the Γ point are very close to the Fermi level. Considering the presence of time reversal symmetry T and mirror symmetry σ_h (orthogonal to the C_3 axis) in $A_2Cr_3As_3$, the TP fermions in current compounds belong to type A[14], which is accompanied by one Weyl nodal line instead of four in type B[15,42]. Including SOC, along the C_3 rotation axis, the singly degenerate band (Λ_5 or Λ_6 state) belongs to the 1D representation of C_{3v} symmetry, while the doubly degenerate bands (Λ_4 state) form the two-dimensional representation, and these TPs along k_z are due to band inversion between the Λ_5/Λ_6 state and the Λ_4 state. Around the Fermi level, band inversion occurs for α, β, and γ bands in $Na_2Cr_3As_3$ (Fig. 4a) as well as α and β in $K_2Cr_3As_3$ (see Supplementary Fig. 2), and these TPs are protected by the C_{3v} symmetry. We compare the band structures of $A_2Cr_3As_3$ along k_z (Supplementary Fig. 2) as well as TPs and (010) surface states (see Supplementary Fig. 3a–c). Owing to the overwhelming bulk states, only the surface states in $Na_2Cr_3As_3$ can be clearly distinguished from the bulk band continuum, resulting in clear Fermi arc structures on the (010) surface (Fig. 4b, c). We also performed calculations using the modified Becke–Johnson (mBJ) potentials[43] and obtained results similar to that of Perdew, Burke, and Ernzerhoff (PBE) for $Na_2Cr_3As_3$ (for details, see "Methods" below). In $K_2Cr_3As_3$, however, the Λ_4 state near ϵ_F, which is lower than Λ_5 and Λ_6 states in PBE calculations (see Supplementary Fig. 2b), is now elevated higher around Γ points, leading to extra band

inversions between β and γ band and hence two new TPs (located at $\epsilon_F + 90$ and $\epsilon_F - 22$ meV), as shown in Fig. 4d. Figure 4b, c, e, f show the surface states in $Na_2Cr_3As_3$ (PBE results) and $K_2Cr_3As_3$ (mBJ results), respectively. For both of these two compounds, two surface states, SS_1 and SS_2, emerge from two TPs (TP_1 and TP_2) near the Γ point, respectively, while the surface states from the TPs (TP_3 and TP_4 in $Na_2Cr_3As_3$, TP_3 in $K_2Cr_3As_3$) away from Γ point are mixed with surrounding bulk states and cannot be easily distinguished. The iso-energy surface states at TP_1 in $Na_2Cr_3As_3$ ($\epsilon_F + 8$ meV) and $K_2Cr_3As_3$ ($\epsilon_F + 90$ meV) are shown in Fig. 4c, f. Akin to ZrTe family of compounds, the TPs (TP_1 in $Na_2Cr_3As_3$ and $K_2Cr_3As_3$) marked as blue (Fig. 4c) and red (Fig. 4f) dots are connected by double 1D Fermi arcs on the (010) surface. We note that, for $K_2Cr_3As_3$, the number of TPs are different in PBE and mBJ calculations. Nevertheless, as long as the band inversions between the Λ_4 and Λ_5 (Λ_6) exist, these intrinsic TPs will be protected by the extra global symmetry (C_{3v}). In the next section, we will further discuss the dynamic correlation effect due to the spin fluctuation on these TPs.

Spin fluctuations and multiorbital susceptibilities

The imaginary part of the bare electron susceptibility χ_0 of $K_2Cr_3As_3$ exhibited a strong peak at the Γ point[30]. In order to investigate the variation of electron susceptibility, we also calculate susceptibility χ_0 using the Lindhard response function for all compounds of this family. As shown in Fig. 5a, b, the bare susceptibilities of $Na_2Cr_3As_3$, $Rb_2Cr_3As_3$, and $Cs_2Cr_3As_3$ resemble that of $K_2Cr_3As_3$. Specifically, the real part χ_0' is relatively featureless, while the imaginary part χ_0'' is dominated by a resonance peak at the Γ point. As reported in previous NMR studies[24,25,32], there were clear differences in the Knight shift and NMR relaxation rate ($1/T_1T$) of $K_2Cr_3As_3$ ($Rb_2Cr_3As_3$) and $Cs_2Cr_3As_3$, implying that the spin susceptibility of $K_2Cr_3As_3$ ($Rb_2Cr_3As_3$) strikingly differs from that of $Cs_2Cr_3As_3$. Therefore, electron–electron interactions must be taken into consideration to explain the aforementioned NMR experiments. We calculate both spin and charge susceptibilities within RPA with intra-orbital Coulomb (U), inter-orbital Coulomb (U'), Hund's coupling (J), and pair-hopping (J') interactions involved (see Supplementary Method for details). In Fig. 5c–f, the real part of charge (spin) susceptibility χ_c' (χ_s') is presented for $U = 2$ eV and $J = 0.3$ eV in comparison to that of bare ones. For all members in this family, the spin susceptibilities are significantly enhanced, while the charge susceptibilities are suppressed. The sharp peak present at the Γ point of $K_2Cr_3As_3$ indicates that it is very close to the critical point with certain values of U and J. Naively, using the simplest
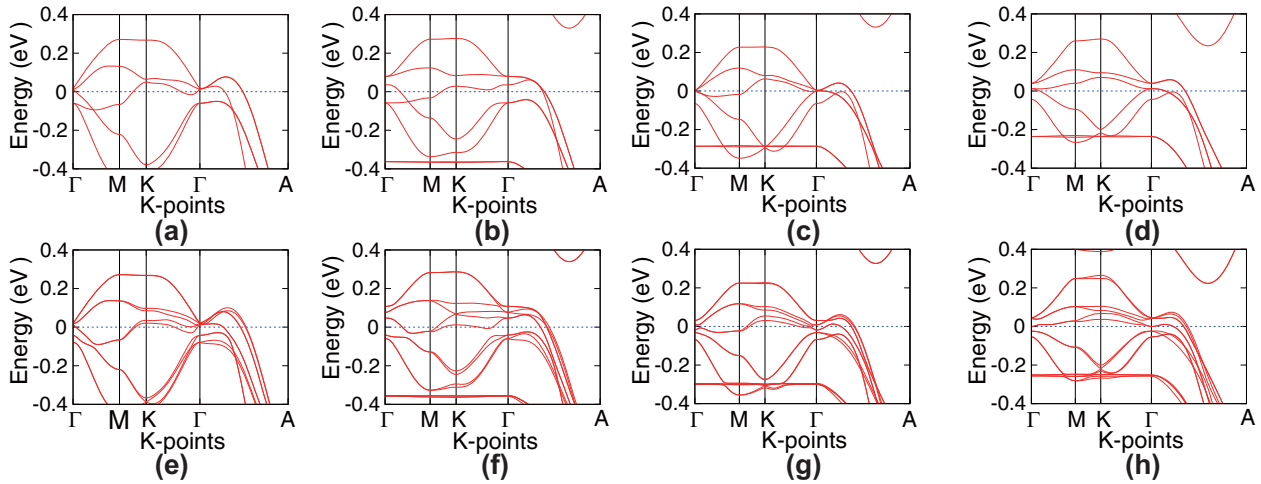
Fig. 2 Electronic band structure of A$_2$Cr$_3$As$_3$. a, e A = Na; **b, f** A = K; **c, g** A = Rb; **d, h** A = Cs. The upper/lower panels are results without/with spin–orbit coupling.

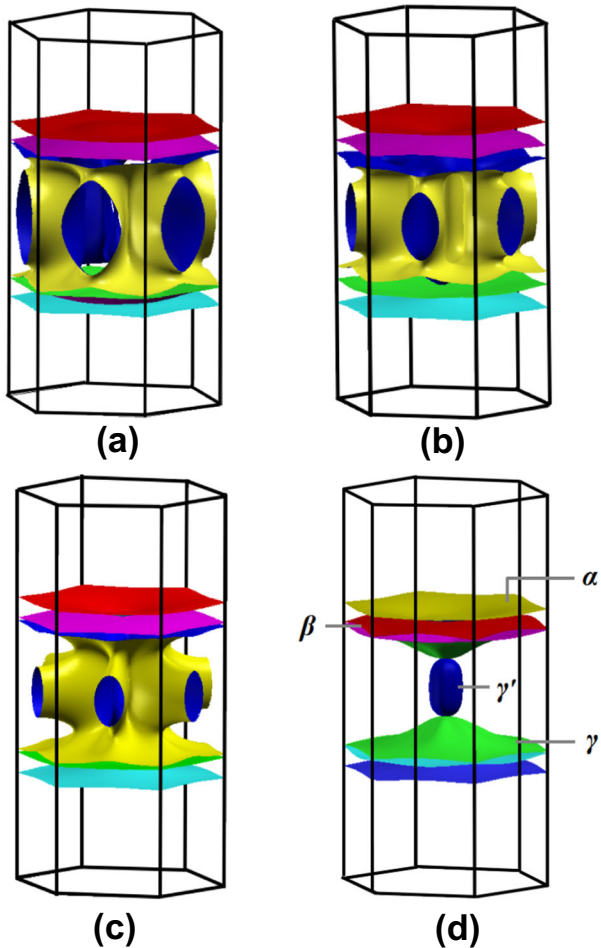**Fig. 3 Fermi-surface sheets of A$_2$Cr$_3$As$_3$. a** Na$_2$Cr$_3$As$_3$, **b** K$_2$Cr$_3$As$_3$, **c** Rb$_2$Cr$_3$As$_3$, and **d** Cs$_2$Cr$_3$As$_3$. In Na$_2$Cr$_3$As$_3$, K$_2$Cr$_3$As$_3$, and Rb$_2$Cr$_3$As$_3$, there are two Q1D FSs and one 3D FS, whereas in Cs$_2$Cr$_3$As$_3$ one more FS emerges.

approximation, the enhancement of the imaginary part χ'' can be written as $\chi''(\mathbf{q}, \omega) \approx \chi_0(\mathbf{q}, \omega) / \left[1 - \overline{U}\chi'_0(\mathbf{q}, \omega)\right]^2$ [44,45], where $\overline{U}$ is the Stoner factor. Applying this approximation, the imaginary part χ'' of K$_2$Cr$_3$As$_3$ is also expected to be strongly enhanced at the

Γ point when $1 - U\chi'_0(\mathbf{q}, \omega)$ approaches zero. The scattering peak of χ' in Rb$_2$Cr$_3$As$_3$ still locates at the Γ point but is lower and broader compared to K$_2$Cr$_3$As$_3$. In the case of Cs$_2$Cr$_3$As$_3$ (Na$_2$Cr$_3$As$_3$), in contrast, only a broadened and plateau-like structure can be found around the $M(\pi, 0, 0)$ and $K\left(\frac{2}{3}\pi, \frac{2}{3}\pi, 0\right)$ points. Interestingly, there exists another broad hump around $Q^* = (0, 0, 0.6\pi)$ in Cs$_2$Cr$_3$As$_3$, which is possibly due to intraband scattering within the γ band. Similar to previous report in iron-based superconductor LaOFeAs[46], such a broad hump might be related to spin–density–wave (SDW) fluctuations. In K$_2$Cr$_3$As$_3$ (Rb$_2$Cr$_3$As$_3$), the SDW hump at Q^* also exists but not apparent, overwhelmed by the large peak located at $\mathbf{q}(0, 0, 0)$. It is worth noting that the strong peak of χ' at the Γ point of K$_2$Cr$_3$As$_3$ (Rb$_2$Cr$_3$As$_3$) is robust against the Hund's coupling (J). It will also be present even if the Hund's coupling is completely turned off ($J = 0$). In addition, the spin susceptibility appears to be insensitive to either the inter-orbital Coulomb repulsion (U') or the pair-hopping interaction (J').

Considering the striking difference in χ'_s between K$_2$Cr$_3$As$_3$ and Cs$_2$Cr$_3$As$_3$, we analyze the dynamic spin susceptibility of these two compounds at the Γ, M, and Q^* points as shown in Fig. 6a, b. The spin susceptibility exhibits a larger enhancement at the Γ point in K$_2$Cr$_3$As$_3$, while in Cs$_2$Cr$_3$As$_3$ the spin susceptibility seems to be more enhanced at a finite $\mathbf{q}$. For all members in this family, we further compare the enhancement of spin susceptibility χ'_s and χ''_s at $\mathbf{q} = (0,0,0)$ in Fig. 6c, d. The results show that the enhancement is most significant in K$_2$Cr$_3$As$_3$, followed by Rb$_2$Cr$_3$As$_3$ and Cs$_2$Cr$_3$As$_3$. Such a systematic trend can also be found in the temperature-dependent spin suscept-ibility enhancement (Fig. 6e, f). Note that the enhancement of χ'' is always larger than that of χ' for both the T- and U-dependent spin susceptibilities, indicating that the system is away from an FM ordered state.

We now consider the NMR relaxation rate $1/T_1T$. It is proportional to $\frac{1}{N}\sum_{\mathbf{q}} \frac{A(\mathbf{q})\text{Im}[\chi(\mathbf{q}, \omega, T)]}{\omega}$, where $A(\mathbf{q})$ is a geometrical structure factor. We chose $A(\mathbf{q}) = 1$ since the geometrical structure factor has little effect on $1/T_1T$[47]. The NMR frequency ω is close to zero, which is chosen to be 1×10^{-5} eV in our calculation. Intriguingly, if we assume that the NMR relaxation rate $1/T_1T$ is dominated by the imaginary part of the spin susceptibility at $\mathbf{q} = 0$ (or the so-called long wavelength approximation[48,49]), the calculated $1/T_1T$ for Na$_2$Cr$_3$As$_3$, K$_2$Cr$_3$As$_3$, and Rb$_2$Cr$_3$As$_3$ (Fig. 6e, f) are qualitatively similar to the NMR experiments of[24,25,31], although such a Curie–Weiss-like temperature dependence is more accurate within a self-consistent renormalization theory[50].
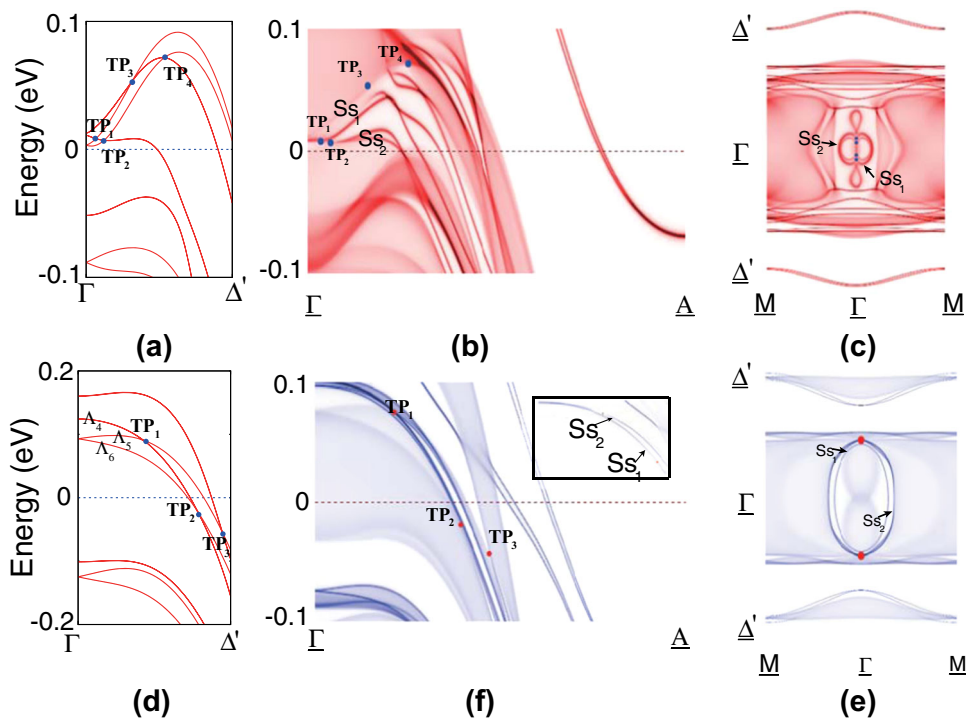
Fig. 4 Electronic band structure and the (010) surface state along k_z. a–c Na$_2$Cr$_3$As$_3$ within PBE calculation. **d, e** K$_2$Cr$_3$As$_3$ within mBJ calculation. The triply degenerate points are marked as solid dots. The iso-energy surface state is located at ϵ_F+8 meV for Na$_2$Cr$_3$As$_3$ and at ϵ_F+90 meV for K$_2$Cr$_3$As$_3$. The inset of **f** shows surface states only, emerging from TP$_1$ and TP$_2$ separately without the bulk states.
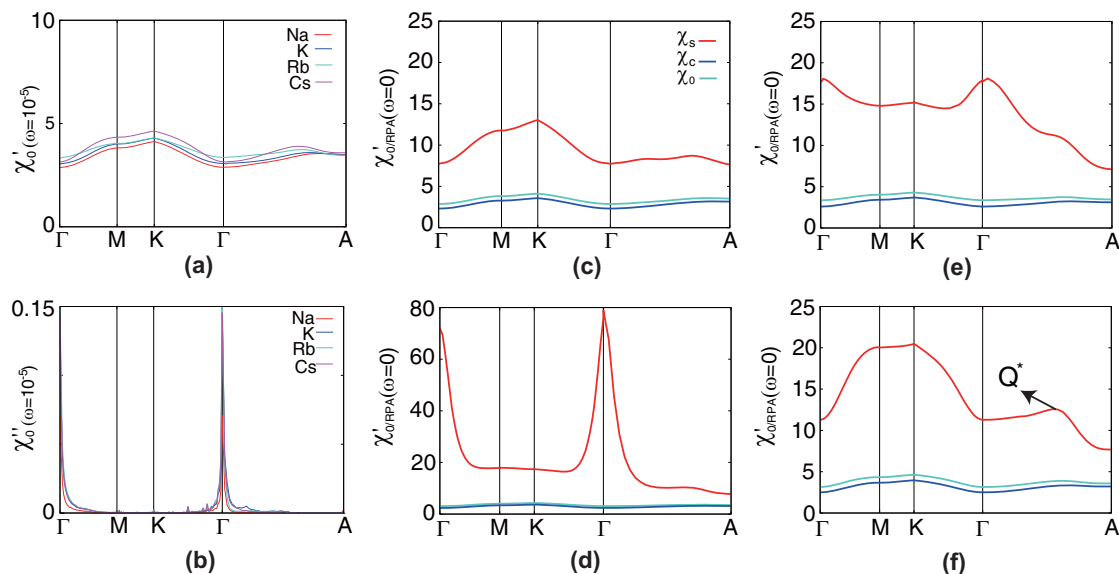
Fig. 5 Electron susceptibility of A$_2$Cr$_3$As$_3$. a Real and **b** imaginary part of the bare electron susceptibility of the A$_2$Cr$_3$As$_3$ family. **c–f** The real part of magnetic susceptibility calculated at the RPA level for **c** Na$_2$Cr$_3$As$_3$, **d** K$_2$Cr$_3$As$_3$, **e** Rb$_2$Cr$_3$As$_3$, and **f** Cs$_2$Cr$_3$As$_3$, respectively. The red, blue, and cyan solid line are spin, charge, and bare (in comparison) susceptibilities, respectively, along high symmetry lines for the compounds of this family with $U = 2.0$ eV and $J = 0.3$ eV.

Nevertheless, in contrast to K$_2$Cr$_3$As$_3$ and Rb$_2$Cr$_3$As$_3$, the enhancement of the spin susceptibility in Cs$_2$Cr$_3$As$_3$ (Fig. 6e, f) exhibits a weak temperature dependence. This implies that the large enhancement of the spin susceptibility at the Γ point is substantially suppressed in Cs$_2$Cr$_3$As$_3$, consistent with ref. [32]. Similar T dependence of the spin susceptibility were also obtained by Graser et al. in LaFeAsO[47] and 26% Co-doped BaFe$_2$As$_2$[51].

It is also informative to consider the impact of FM fluctuation on the electronic band structure. As the spin fluctuation is most significant for K$_2$Cr$_3$As$_3$ in our calculations, we calculated its dynamic RPA self-energy $\Sigma(\omega)$ (see Supplementary Fig. 4) and obtained its dynamic correlated electronic spectrum. In Fig. 7, we show the renormalized quasi-particle energy spectrum. Away from the Fermi level, we see significantly increased scattering rate, most
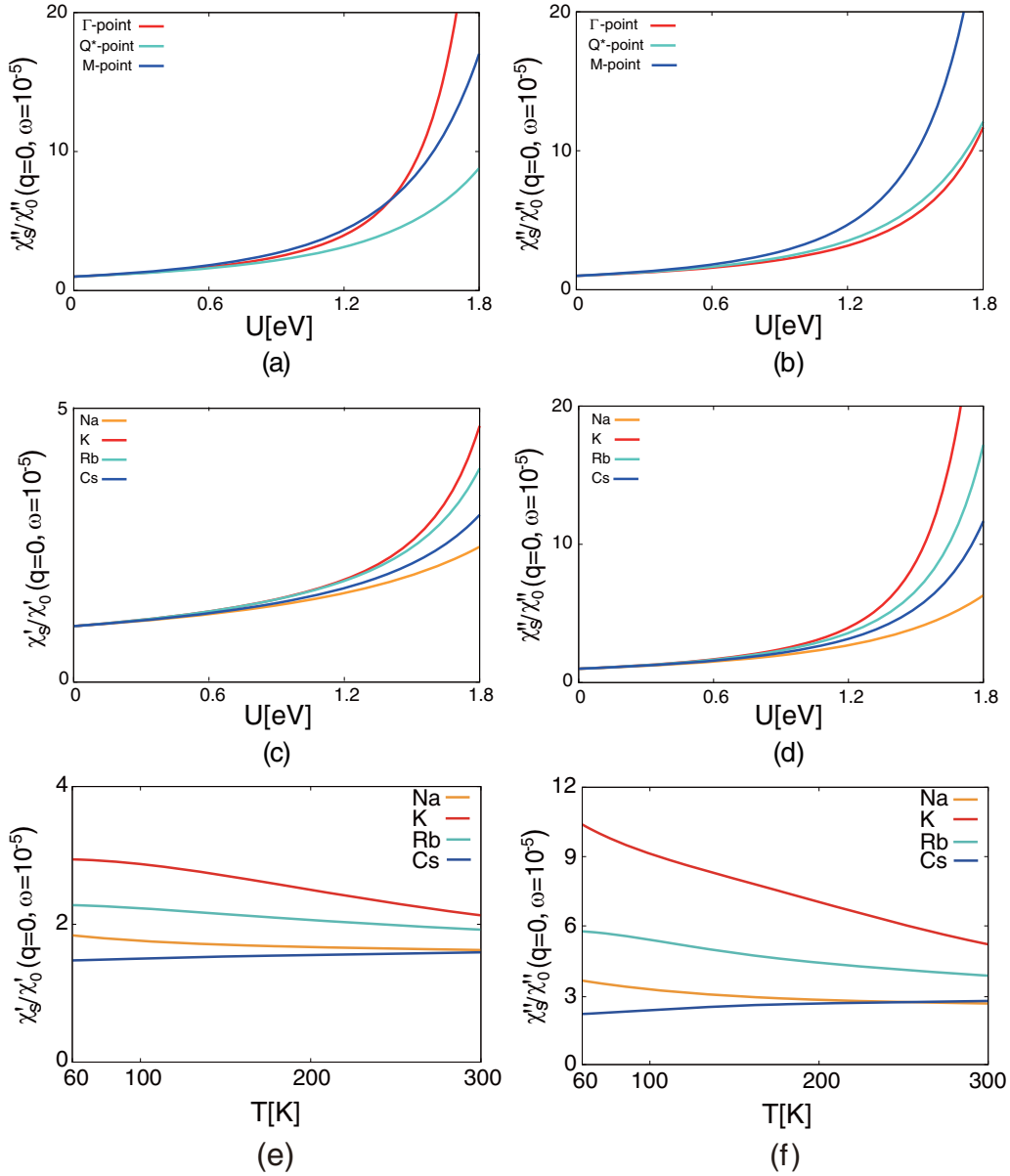
Fig. 6 Comparison of spin susceptibility. a, b Imaginary part of the spin susceptibility (χ_s/χ_0) at Γ, M, and Q^* (marked in Fig. 5f) for **a** $K_2Cr_3As_3$ and **b** $Cs_2Cr_3As_3$, respectively. **c, d** show **c** the real and **d** imaginary part of the spin susceptibility (χ_s/χ_0) at Γ as a function of intra-orbital Coulomb interaction U for $A_2Cr_3As_3$ (A = Na, K, Rb, and Cs). **e, f** Real and imaginary part of the spin susceptibility (χ_s/χ_0) as a function of temperature at Γ of $A_2Cr_3As_3$. The interaction parameters have been chosen to be $U = 1.2$ eV and $J = 0.2\,U$, and the results for other interaction region ($U < U_c$) are similar.

prominent close to A around $E_F - 0.4$ eV. However, the renormalization to the quasi-particle states close to the Fermi level is negligible within RPA. Thus the TPs remain and are only slightly shifted in $K_2Cr_3As_3$. Our results are in agreement with previous theoretical studies that correlation effect may be greatly reduced owing to the formation of molecular orbitals[52–55] and are in line with the experimental observation that no appreciable magnetic local moment is found in these systems. In addition, the comparison between the RPA and PBE results also illustrates that the dynamic RPA self-energy has little effect on the existence of TPs in these systems. Despite of its moderate effect at normal state, the FM fluctuation would influence the topological properties in superconducting state by allowing for the nontrivial spin–triplet pairing (p- or f-wave), as has been conjectured theoretically[52–56] and investigated experimentally[22–25,57].

DISCUSSION

In the normal state, the TP topological metal has been regarded as the intermediate phase between Dirac and Weyl semimetals[14]. The TPs can split into Weyl points by breaking σ_v containing the C_3 axis or merge into Dirac point after imposing inversion symmetry. Although the 233-type $A_2Cr_3As_3$ is absent of an inversion center, the 133-type ACr_3As_3 is centrosymmetric. It is interesting to notice that a Dirac-like crossing point appears between the α and β bands along k_z in the recently reported $KHCr_3As_3$[58,59]. In $Na_2Cr_3As_3$, the surface state lies only 8 meV above the Fermi level, and it is possible for this surface state to become superconducting through proximity effect. In experiment, such a surface superconducting state might have influence on the in-plane H_{c2}[60], although such a possibility has been ruled out in $K_2Cr_3As_3$[57,61]. One possible reason is that the surface state is far away from the Fermi level in stoichiometric $K_2Cr_3As_3$.
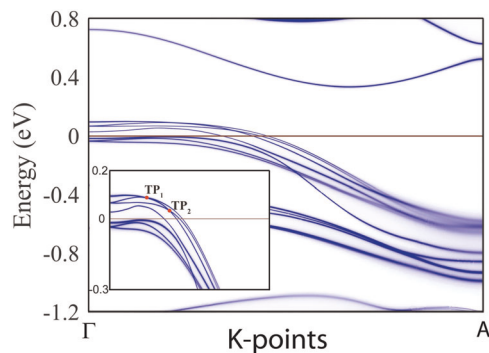
Fig. 7 The RPA renormalized quasi-particle spectrum of $K_2As_3Cr_3$ based on PBE results. Around the Fermi level, the dynamic correlation has relative small effect on the quasi-particle spectrum. The inset shows the same spectrum with smaller energy range. The triply degenerate points are marked as red solid dots.

In the superconducting state, lacking inversion symmetry gives rise to Rashba-type ASOC interactions so that the single-particle Hamiltonian takes the form $h(\mathbf{k}) = \xi(\mathbf{k})\sigma_0 + \mathbf{g_k}\cdot\boldsymbol{\sigma}$. With an extra parity-breaking term $\mathbf{g_k}\cdot\boldsymbol{\sigma}$, the mixture of singlet and triplet pairing is allowed and the order parameter takes the general form $\Delta(\mathbf{k}) = \Psi_{\mathbf{k}}\sigma_0 + \mathbf{d_k}\cdot\boldsymbol{\sigma}$, where $\Psi_{\mathbf{k}} = \Psi_{-\mathbf{k}}$ and $\mathbf{d_k} = -\mathbf{d_{-k}}$. The triplet pairing state can be stable as long as $\mathbf{d_k}$ is parallel to $\mathbf{g_k}$[62]. In the following, we discuss the possible nontrivial topological property in superconducting state by the symmetry analysis of super-conducting gap $\Delta(\mathbf{k})$ and the spin–orbit coupling $\mathbf{g_k}$. First, considering the gap symmetry, the large FM fluctuations favor the spin–triplet pairing component than the spin-singlet one. For the gap, symmetry belongs to the A'' representation of D_{3h} group (e.g., p_z-wave[53]), $\Delta(\mathbf{k})$ satisfies $U_{\mathbf{k}}(S_6)\Delta(\mathbf{k})U_{-\mathbf{k}}(S_6)^T = \chi_{S_6}\Delta_{S_6}(\mathbf{k})$, where $\chi_{S_6} = -1$ and the sixfold rotoinversion symmetry $S_6 = iC_6$. We calculate the $\mathbb{Z}_6$ indexes (z_6' and z_6'') associated with the S_6 according to the symmetry indicators for topological super-conductors defined in refs [63,64]. The resulting z_6' and z_6'' are both nonzeros ($z_6' = 1$ and $z_6'' = -1$) for mBJ results of $Na_2Cr_3As_3$ and $K_2Cr_3As_3$ (see Supplementary Table 1 for details). Second, consider-ing the large 3D FS around the Γ point in $K_2Cr_3As_3$ ($Rb_2Cr_3As_3$), the corresponding representation of D_{3h} is Γ_7 (Γ_8), yielding $\mathbf{g_k} = \beta_1 k_z\left[\left(k_x^2 - k_y^2\right)\sigma_x - 2k_x k_y\sigma_y\right] + \beta_2 k_x\left(k_x^2 - 3k_y^2\right)\sigma_z$[65], where β_1 and β_2 are linear combination coefficients. Moreover, the ASOC splitting around $K(\frac{2}{3}\pi, \frac{2}{3}\pi, 0)$ is roughly 60 meV[30], while along A(0, 0, π)–H(π, 0, π) it is nearly negligible. Therefore the ASOC splitting should be dominated by the β_2 term, i.e., $\mathbf{g_k} = k_x\left(k_x^2 - 3k_y^2\right)\sigma_z$, and thus it is invariant under $\mathbf{g}_{k_i,+k_0} = \mathbf{g}_{k_i,-k_0}$. It has been demonstrated by Schnyder et al. [16] that the presence of such type of symmetry gives rise to topological nontrivial features of line nodes in the gap of NCSs. More importantly, the Majorana surface states can exist at time-reversal-invariant momenta of the surface Brillouin zone. Since in the non-superconducting state the 1D arc surface states connecting the TPs already exist, it will be more interesting to further investigate the topological properties in the superconducting state of $A_2Cr_3As_3$.

In summary, we have performed first-principles calculations on $A_2Cr_3As_3$ (A = Na, K, Rb and Cs) and analyzed the systematic variations of electronic structures, FSs, topological properties, and magnetic spin susceptibilities of the compounds in this family. Using the surface Green's function method, we calculate the (010) surface state and find that the TPs in $Na_2Cr_3As_3$ and $K_2Cr_3As_3$ are connected by double 1D Fermi arcs. To explore the behavior of magnetic spin response, charge and spin susceptibility are obtained by employing RPA calculations. We demonstrate that the strong enhancement of spin fluctuations is present at the Γ point in $K_2Cr_3As_3$ and $Rb_2Cr_3As_3$, while in $Cs_2Cr_3As_3$ and $Na_2Cr_3As_3$, the FM spin fluctuations are not apparently enhanced. The existence of TPs is robust against the FM spin fluctuation under RPA. Based on symmetry analysis, the $A_2Cr_3As_3$ compounds are possible candidates for topological superconductor.

Note added

During the preparation of our manuscript, we became aware of a recent paper[66]. In addition to the scenario we discussed here, they have proposed that triplet p_z-pairing can also be topological superconductors with weak SOC.

METHODS

Calculation parameters

The calculations were carried out using density functional theory as implemented in the Vienna Abinitio Simulation Package[67,68]. The PBE parameterization of generalized gradient approximation to the exchange correlation functional was employed[69]. The energy cutoff of the plane-wave basis was up to 450 eV, and a $6 \times 6 \times 12$ Γ-centered Monkhorst–Pack[70] k-point mesh was chosen to ensure that the total energy converges to 1 meV/cell. We also performed a comparison with the mBJ exchange potentials[43] for $Na_2Cr_3As_3$ and $K_2Cr_3As_3$.

Structural parameters

The calculations of $K_2Cr_3As_3$, $Rb_2Cr_3As_3$, and $Cs_2Cr_3As_3$ were performed with experimental crystal structure. For $Na_2Cr_3As_3$, only the lattice constants are available from experiment, therefore we employed its lattice constants from experiment, while the atomic positions are fully relaxed with dynamical mean-field theory at 300 K[71,72].

Tight binding (TB) Hamiltonian

The band structures obtained with the PBE and the mBJ methods were fitted to a TB model Hamiltonian with maximally projected Wannier function method[73,74] using 48 atomic orbitals including Cr $3d$ and As $4p$. The resulting Hamiltonian was then used to calculate the FS, charge (spin) susceptibility, self-energy, and surface state with surface Green's function[75].

DATA AVAILABILITY

The data that support the findings of this study are available from the corresponding author upon reasonable request.

CODE AVAILABILITY

The computer code to perform RPA calculations is available from the corresponding author upon reasonable request.

REFERENCES

1. Qi, X.-L. & Zhang, S.-C. Topological insulators and superconductors. *Rev. Mod. Phys.* **83**, 1057–1110 (2011).
2. Zhang, H. et al. Topological insulators in Bi_2Se_3, Bi_2Te_3 and Sb_2Te_3 with a single Dirac cone on the surface. *Nat. Phys.* **5**, 438 (2009).
3. Hasan, M. Z. & Kane, C. L. Colloquium: Topological insulators. *Rev. Mod. Phys.* **82**, 3045–3067 (2010).
4. Wan, X., Turner, A. M., Vishwanath, A. & Savrasov, S. Y. Topological semimetal and fermi-arc surface states in the electronic structure of pyrochlore iridates. *Phys. Rev. B* **83**, 205101 (2011).
5. Weng, H., Fang, C., Fang, Z., Bernevig, B. A. & Dai, X. Weyl semimetal phase in noncentrosymmetric transition-metal monophosphides. *Phys. Rev. X* **5**, 011029 (2015).
6. Lv, B. Q. et al. Experimental discovery of weyl semimetal TaAs. *Phys. Rev. X* **5**, 031013 (2015).

7. Wang, Z. et al. Dirac semimetal and topological phase transitions in A_3Bi (A = Na, K, Rb). *Phys. Rev. B* **85**, 195320 (2012).

8. Wang, Z., Weng, H., Wu, Q., Dai, X. & Fang, Z. Three-dimensional dirac semimetal and quantum transport in Cd_3As_2. *Phys. Rev. B* **88**, 125427 (2013).

9. Liu, Z. et al. Discovery of a three-dimensional topological dirac semimetal, Na_3Bi. *Science* **343**, 864–867 (2014).

10. Borisenko, S. et al. Experimental realization of a three-dimensional dirac semimetal. *Phys. Rev. Lett.* **113**, 027603 (2014).

11. Burkov, A. A., Hook, M. D. & Balents, L. Topological nodal semimetals. *Phys. Rev. B* **84**, 235126 (2011).

12. Yu, R., Weng, H., Fang, Z., Dai, X. & Hu, X. Topological node-line semimetal and dirac semimetal state in antiperovskite Cu_3PdN. *Phys. Rev. Lett.* **115**, 036807 (2015).

13. Weng, H. et al. Topological node-line semimetal in three-dimensional graphene networks. *Phys. Rev. B* **92**, 045108 (2015).

14. Zhu, Z., Winkler, G. W., Wu, Q., Li, J. & Soluyanov, A. A. Triple point topological metals. *Phys. Rev. X* **6**, 031003 (2016).

15. Winkler, G. W., Wu, Q., Troyer, M., Krogstrup, P. & Soluyanov, A. A. Topological phases in $InAs_{1-x}Sb_x$: From novel topological semimetal to majorana wire. *Phys. Rev. Lett.* **117**, 076403 (2016).

16. Schnyder, A. P., Brydon, P. M. R. & Timm, C. Types of topological surface states in nodal noncentrosymmetric superconductors. *Phys. Rev. B* **85**, 024522 (2012).

17. Agterberg, D. F., Brydon, P. M. R. & Timm, C. Bogoliubov fermi surfaces in superconductors with broken time-reversal symmetry. *Phys. Rev. Lett.* **118**, 127001 (2017).

18. Schnyder, A. P. & Brydon, P. M. Topological surface states in nodal superconductors. *J. Phys. Condens. Matter* **27**, 243201 (2015).

19. Schnyder, A. P. & Ryu, S. Topological phases and surface flat bands in superconductors without inversion symmetry. *Phys. Rev. B* **84**, 060504 (2011).

20. Brydon, P. M. R., Schnyder, A. P. & Timm, C. Topologically protected flat zero-energy surface bands in noncentrosymmetric superconductors. *Phys. Rev. B* **84**, 020501 (2011).

21. Matsuura, S., Chang, P.-Y., Schnyder, A. P. & Ryu, S. Protected boundary states in gapless topological phases. *N. J. Phys.* **15**, 065001 (2013).

22. Pang, G. et al. Evidence for nodal superconductivity in quasi-one-dimensional $K_2Cr_3As_3$. *Phys. Rev. B* **91**, 220502 (2015).

23. Pang, G. et al. Penetration depth measurements of $K_2Cr_3As_3$ and $Rb_2Cr_3As_3$. *J. Magn. Magn. Mater.* **400**, 84–87 (2016).

24. Zhi, H. Z., Imai, T., Ning, F. L., Bao, J.-K. & Cao, G.-H. Nmr investigation of the quasi-one-dimensional superconductor $K_2Cr_3As_3$. *Phys. Rev. Lett.* **114**, 147004 (2015).

25. Yang, J., Tang, Z. T., Cao, G. H. & Zheng, G.-q Ferromagnetic spin fluctuation and unconventional superconductivity in $Rb_2Cr_3As_3$ revealed by ^{75}As NMR and NQR. *Phys. Rev. Lett.* **115**, 147002 (2015).

26. Adroja, D. T. et al. Superconducting ground state of quasi-one-dimensional $K_2Cr_3As_3$ investigated using μSR measurements. *Phys. Rev. B* **92**, 134505 (2015).

27. Adroja, D. et al. Nodal superconducting gap structure in the quasi-one-dimensional $Cs_2Cr_3As_3$ investigated using μSR measurements. *J. Phys. Soc. Jpn.* **86**, 044710 (2017).

28. Shao, Y. T. et al. Evidence of line nodes in superconducting gap function in $K_2Cr_3As_3$ from specific-heat measurements. *EPL (Europhys. Lett.)* **123**, 57001 (2018).

29. Tang, Z.-T. et al. Unconventional superconductivity in quasi-one-dimensional $Rb_2Cr_3As_3$. *Phys. Rev. B* **91**, 020506 (2015).

30. Jiang, H., Cao, G. & Cao, C. Electronic structure of quasi-one-dimensional superconductor $K_2Cr_3As_3$ from first-principles calculations. *Sci. Rep.* **5**, 16054 EP (2015).

31. Luo, J. et al. Tuning the distance to a possible ferromagnetic quantum critical point in $A_2Cr_3As_3$. *Phys. Rev. Lett.* **123**, 047001 (2019).

32. Zhi, H. et al. ^{133}Cs and ^{75}As nmr investigation of the normal metallic state of quasi-one-dimensional $Cs_2Cr_3As_3$. *Phys. Rev. B* **93**, 174508 (2016).

33. Mu, Q.-G. et al. Ion-exchange synthesis and superconductivity at 8.6 K of $Na_2Cr_3As_3$ with quasi-one-dimensional crystal structure. *Phys. Rev. Mater.* **2**, 034803 (2018).

34. Bao, J.-K. et al. Superconductivity in quasi-one-dimensional $K_2Cr_3As_3$ with significant electron correlations. *Phys. Rev. X* **5**, 011013 (2015).

35. Wang, X. et al. Tunable electronic anisotropy in single-crystal $A_2Cr_3As_3$ (A = K, Rb) quasi-one-dimensional superconductors. *Phys. Rev. B* **92**, 020508 (2015).

36. Tang, Z.-T. et al. Superconductivity in quasi-one-dimensional $Cs_2Cr_3As_3$ with large interchain distance. *Sci. China Mater.* **58**, 16–20 (2015).

37. Bao, J.-K. et al. Cluster spin-glass ground state in quasi-one-dimensional KCr_3As_3. *Phys. Rev. B* **91**, 180404 (2015).

38. Mu, Q.-G. et al. Superconductivity at 5 K in quasi-one-dimensional Cr-based KCr_3As_3 single crystals. *Phys. Rev. B* **96**, 140504 (2017).

39. Tang, Z.-T. et al. Synthesis, crystal structure and physical properties of quasi-one-dimensional ACr_3As_3 (A = Rb, Cs). *Sci. China Mater.* **58**, 543–549 (2015).

40. Liu, T. et al. Superconductivity at 7.3 K in the 133-type Cr-based $RbCr_3As_3$ single crystals. *EPL (Europhys. Lett.)* **120**, 27006 (2018).

41. Xian-Xin, W., Cong-Cong, L., Jing, Y., Heng, F. & Jiang-Ping, H. Magnetism in quasi-one-dimensional $A_2Cr_3As_3$ (A = K, Rb) superconductors. *Chin. Phys. Lett.* **32**, 057401 (2015).

42. Zaheer, S. et al. Spin texture on the fermi surface of tensile-strained HgTe. *Phys. Rev. B* **87**, 045202 (2013).

43. Tran, F. & Blaha, P. Accurate band gaps of semiconductors and insulators with a semilocal exchange-correlation potential. *Phys. Rev. Lett.* **102**, 226401 (2009).

44. Pavarini, E. & Mazin, I. I. NMR relaxation rates and knight shifts in MgB_2. *Phys. Rev. B* **64**, 140504 (2001).

45. Shastry, B. S. & Abrahams, E. What does the Korringa ratio measure? *Phys. Rev. Lett.* **72**, 1933–1936 (1994).

46. Korshunov, M. M. & Eremin, I. Theory of magnetic excitations in iron-based layered superconductors. *Phys. Rev. B* **78**, 140509 (2008).

47. Graser, S., Maier, T. A., Hirschfeld, P. J. & Scalapino, D. J. Near-degeneracy of several pairing channels in multiorbital models for the Fe pnictides. *N. J. Phys.* **11**, 025016 (2009).

48. Moriya, T. & Kawabata, A. Effect of spin fluctuations on itinerant electron ferromagnetism. *J. Phys. Soc. Jpn.* **34**, 639–651 (1973).

49. Moriya, T. & Ueda, K. Nuclear magnetic relaxation in weakly ferro-and antiferromagnetic metals. *Solid State Commun.* **15**, 169–172 (1974).

50. Moriya, T. in *Spin Fluctuations in Itinerant Electron Magnetism* 82–108 (Springer, 1985).

51. Ning, F. L. et al. Contrasting spin dynamics between underdoped and overdoped $Ba(F_{1-x}Co_x)_2As_2$. *Phys. Rev. Lett.* **104**, 037001 (2010).

52. Zhou, Y., Cao, C. & Zhang, F.-C. Theory for superconductivity in alkali chromium arsenides $A_2Cr_3As_3$ (A = K, Rb, Cs). *Sci. Bull.* **62**, 208–211 (2017).

53. Wu, X., Yang, F., Le, C., Fan, H. & Hu, J. Triplet p_z-wave pairing in quasi-one-dimensional $A_2Cr_3As_3$ superconductors (A = K, Rb, Cs). *Phys. Rev. B* **92**, 104511 (2015).

54. Zhong, H., Feng, X.-Y., Chen, H. & Dai, J. Formation of molecular-orbital bands in a twisted hubbard tube: implications for unconventional superconductivity in $K_2Cr_3As_3$. *Phys. Rev. Lett.* **115**, 227001 (2015).

55. Miao, J.-J., Zhang, F.-C. & Zhou, Y. Instability of three-band tomonaga-luttinger liquid: Renormalization group analysis and possible application to $K_2Cr_3As_3$. *Phys. Rev. B* **94**, 205129 (2016).

56. Zhang, L.-D., Wu, X., Fan, H., Yang, F. & Hu, J. Revisitation of superconductivity in $K_2Cr_3As_3$ based on the six-band model. *EPL (Europhys. Lett.)* **113**, 37003 (2016).

57. Zuo, H. et al. Temperature and angular dependence of the upper critical field in $K_2Cr_3As_3$. *Phys. Rev. B* **95**, 014502 (2017).

58. Taddei, K. M. et al. Tuning from frustrated magnetism to superconductivity in quasi-one-dimensional KCr_3As_3 through hydrogen doping. *Phys. Rev. B* **100**, 220503 (2019).

59. Wu, S.-Q., Cao, C. & Cao, G.-H. Lifshitz transition and nontrivial H-doping effect in the Cr-based superconductor $KCr_3As_3H_x$. *Phys. Rev. B* **100**, 155108 (2019).

60. Keller, N., Tholence, J. L., Huxley, A. & Flouquet, J. Angular dependence of the upper critical field of the heavy fermion superconductor UPt_3. *Phys. Rev. Lett.* **73**, 2364–2367 (1994).

61. Cao, G.-H. & Zhu, Z.-W. Superconductivity with peculiar upper critical fields in quasi-one-dimensional Cr-based pnictides. *Chin. Phys. B* **27**, 107401 (2018).

62. Frigeri, P. A., Agterberg, D. F., Koga, A. & Sigrist, M. Superconductivity without inversion symmetry: MnSi versus $CePt_3Si$. *Phys. Rev. Lett.* **92**, 097001 (2004).

63. Ono, S., Yanase, Y. & Watanabe, H. Symmetry indicators for topological superconductors. *Phys. Rev. Res.* **1**, 013012 (2019).

64. Ono, S., Po, H. C. & Watanabe, H. Refined symmetry indicators for topological superconductors in all space groups. Preprint at https://arxiv.org/abs/1909.09634 (2019).

65. Smidman, M., Salamon, M., Yuan, H. & Agterberg, D. Superconductivity and spin-orbit coupling in non-centrosymmetric materials: a review. *Rep. Progr. Phys.* **80**, 036501 (2017).

66. Liu, C.-C. et al. Intrinsic topological superconductivity with exactly flat surface bands in the quasi-one-dimensional A2Cr3As3 (A = Na, K, Rb, Cs) superconductors. Preprint at https://arxiv.org/abs/1909.00943 (2019).

67. Kresse, G. & Hafner, J. Ab initio molecular dynamics for liquid metals. *Phys. Rev. B* **47**, 558–561 (1993).

68. Kresse, G. & Joubert, D. From ultrasoft pseudopotentials to the projector augmented-wave method. *Phys. Rev. B* **59**, 1758–1775 (1999).

69. Perdew, J. P., Burke, K. & Ernzerhof, M. Generalized gradient approximation made simple. *Phys. Rev. Lett.* **77**, 3865–3868 (1996).

70. Monkhorst, H. J. & Pack, J. D. Special points for brillouin-zone integrations. *Phys. Rev. B* **13**, 5188–5192 (1976).

71. Georges, A., Kotliar, G., Krauth, W. & Rozenberg, M. J. Dynamical mean-field theory of strongly correlated fermion systems and the limit of infinite dimensions. *Rev. Mod. Phys.* **68**, 13–125 (1996).

72. Kotliar, G. et al. Electronic structure calculations with dynamical mean-field theory. *Rev. Mod. Phys.* **78**, 865–951 (2006).
73. Mostofi, A. A. et al. wannier90: a tool for obtaining maximally-localised wannier functions. *Comput. Phys. Commun.* **178**, 685–699 (2008).
74. Wang, X., Yates, J. R., Souza, I. & Vanderbilt, D. Ab initio calculation of the anomalous hall conductivity by wannier interpolation. *Phys. Rev. B* **74**, 195118 (2006).
75. Sancho, M. L., Sancho, J. L., Sancho, J. L. & Rubio, J. Highly convergent schemes for the calculation of bulk and surface green functions. *J. Phys. F Metal Phys.* **15**, 851 (1985).

AUTHOR CONTRIBUTIONS

C.X. and C.C. designed research; C.X. performed the calculations; C.X., N.W., Q.C., and C.C. drafted the manuscript; C.X. and C.C. were responsible for the data analysis; all the authors participated in discussions.

COMPETING INTERESTS

The authors declare no competing interests.

ADDITIONAL INFORMATION

Supplementary information is available for this paper at https://doi.org/10.1038/s41524-020-0294-9.

Correspondence and requests for materials should be addressed to C.C. or Q.C.

Reprints and permission information is available at http://www.nature.com/reprints

Publisher's note Springer Nature remains neutral with regard to jurisdictional claims in published maps and institutional affiliations.